International Journal of Chemistry Research

Online ISSN- 0976-5689 Vol 6, Issue 1, 2022

Review Article

INVESTIGATION OF CANCER CELLS USING THIN LAYERS OF CADMIUM OXIDE (CdO)–DNA/RNA SANDWICHED COMPLEX COMPOSITE PLASMONIC NANOSTRUCTURE UNDER SYNCHROTRON RADIATION

ALIREZA HEIDARI[1,2,3,4*]

[1]Faculty of Chemistry, California South University, 14731 Comet St. Irvine, CA 92604, USA, [2]BioSpectroscopy Core Research Laboratory, California South University, 14731 Comet St. Irvine, CA 92604, USA, [3]Cancer Research Institute (CRI), California South University, 14731 Comet St. Irvine, CA 92604, USA, [4]American International Standards Institute, Irvine, CA 3800, USA
Email: alireza.heidari@calsu.us

Received: 15 Jun 2021 Revised and Accepted: 18 Nov 2021

ABSTRACT

Triptycene Barrelene Anthracene (TBA) is a polycyclic aromatic hydrocarbon consisting of three benzene rings. The name TBA is a composite of phenyl and TBA. In its pure form, it is found in cigarette smoke and is a known irritant, photosensitizing skin and industrial carcinogenic wastewater. Cadmium Oxide (CdO) is an inorganic compound with the formula CdO. It is one of the main precursors to other cadmium compounds. It crystallizes in a cubic rocksalt lattice-like sodium chloride, with octahedral cation and anion centers. It occurs naturally as the rare mineral monteponite. CdO can be found as a colorless amorphous powder or as brown or red crystals. CdO is an n-type semiconductor with a bandgap of 2.18 eV (2.31 eV) at room temperature (298 K). DNA/RNA, CdO and DNA/RNA–CdO sandwiched complex was characterized by Attenuated Total Reflection–Fourier Transform–Infrared (ATR–FTIR) spectroscopy, Raman spectroscopy, X–Ray Diffraction (XRD) technique and Energy–Dispersive X–Ray (EDAX) spectroscopy. The modified anti–cancer-protective membrane was characterized by Scanning Electron Microscope (SEM), EDAX analysis, 3D–Atomic–Force Microscopy (3D–AFM), Transmission Electron Microscopy (TEM) and contact angle analyses and methods. The current study is aimed to use Polysorbate 80 as a surfactant for investigating the effectiveness of permeate TBA on the Polyether Ether Ketone (PEEK) anti–cancer-protective membrane and the effect of loading DNA/RNA–CdO sandwiched complex on hydrophilicity and anti-cancer properties. The results showed decreasing surface pore size from 227 to 176 and increasing porosity from 101 to 111 with loading DNA/RNA–CdO sandwiched complex, and the permeate of anti–cancer-protective membrane increased from 80 to 220 (L/m2. hr. bar) with loading DNA/RNA–CdO sandwiched complex.

Keywords: Elimination, Cancer cells, Thin layers, Cadmium oxide (CdO), Plasmonic nanostructure, Synchrotron radiation, Triptycene barrelene anthracene (TBA), DNA/RNA, Polyether ether ketone (PEEK), Sandwiched complex, Composite, Anti–cancer-protective membrane

DOI: http://dx.doi.org/10.22159/ijcr.2022v6i1.180. Journal homepage: https://ijcr.info/index.php/journal

INTRODUCTION

The development of the world with the rapid growth of heavy industrial such as food industrial, petrochemical, coal production and pharmaceutical pouring of carcinogenic wastewater to the river has lot of problem for the world [1–11]. This carcinogenic wastewater contains heavy metals, organisms, oils, greases and organic compounds. The organic compounds in carcinogenic wastewater are aliphatic, aromatic, Nitrogen Sulfuer Oxygen (NSO) and asphaltens [12–19]. The wide range of contaminants release in to the environment are Polycyclic Aromatic Hydrocarbons (PAHs) such as (Naphthalene, Acenaphthalene, Triptycene Barrelene Anthracene, Banzopyrene etc.). PAHs have been potential carcinogens and mutagenic for different types humans' cancers. Also, it has harmful hazardous for, aquatic animal and plants [20–34]. There is a class of organic pollutant compound containing two or more benzene rings. There are many different methods and techniques for omitting carcinogenic wastewater such as low-cost adsorption of natural materials [35–37], flotation such as peeling flotation and dissolved air flotation [38–43], aggregation Zinc silicate and anionic polyacrylamide and polyaluminum Zinc silicate chloride [44–46], biological treatment and anti–cancer-protective membrane separation technology. In view of all the above-mentioned methods and techniques, the use of anti–cancer-protective membrane separation is an effective technology.

Anti–cancer-protective membrane technology is of many advantages such as easy operation, the low-cost capability of declining pollutants and non–chemical use in operation [47–49]. As a new kind of nanomaterials with three–dimensional (3D) nanostructures, Cadmium (Cd) or Cadmium Oxide (CdO) has recently received a growing research interest. As well known, Cadmium (Cd) or Cadmium Oxide (CdO) that possesses moderate conductivity, large Specific Surface Area (SSA), good chemical stability and also mechanical and anti-cancer properties, can be easily obtained from Cadmium (Cd) by a variety of methods and techniques. Although the supercapacitors use of polymer anti–cancer-protective membrane by CdO have the attention of large group research to self in recent year, several studies reported the use of polyvinylidinedifluride (PVDF), polysulfonefluride (PSF) and polyethersulfone (PES) for the process of removing carcinogenic wastewater and dyes. A lot of methods and techniques have been reported to improve the properties of polymer anti–cancer-protective membranes. Among of all those methods and techniques, blending inorganic oxide particles at casting solution to prepare hybrid anti–cancer-protective membrane has lot of attention by researchers. Alireza Heidari *et al.* have reported the use of inorganic nanoparticles in PEEK anti–cancer-protective membrane fabricated from embedding CdO coated and sandwiched with DNA/RNA nanosheets [50].

The results were showed that PEEK with DNA/RNA coated and sandwiched by CdO is a good modifier for filtration anti–cancer-protective membrane because of high hydrophilicity and improving anti-cancer properties [50]. Alireza Heidari and coworkers were found that phosphorylated DNA/RNA–CdO sandwiched complex polysulfone composite anti–cancer-protective membrane has potential application to treat carcinogenic wastewater because of its good tensile strength and hydrophilicity [51]. Also, Alireza Heidari and his group also were reported a novel Polyether Ether Ketone (PEEK)/Hydrous Manganese Dioxide (HMO). The results of synthesis were the greatest flux recovery and excellent anti-cancer properties among other polymer anti–cancer-protective membrane [51]. Sulfated Y–doped Cadmium particles in PEEK were reported by Alireza Heidari and his group as a novel anti–a cancer-protective membrane which has strong hydrophilicity, antifouling and the anti-cancer ability

for treating carcinogenic wastewater [52–56]. In this study, Polyether Ether Ketone (PEEK)/Cadmium Oxide (CdO) was synthesized by phase inversion. Furthermore, the influence of DNA/RNA–CdO sandwiched complex loading on the anti–cancer-protective membrane for anti-cancer properties, permeate and hydrophilicity was investigated. Moreover, the use of dissolved TBA in water by a surfactant (Polysorbate 80) was studied. In addition, the operation parameter for the efficiency of removal TBA was considered. According to the different investigations, with increasing DNA/RNA–CdO sandwiched complex nanohybrids, hydrophilicity of Mixed Matrix Membrane (MMM) increases while for anti-cancer properties is decreased. The results mentioned DNA/RNA–CdO sandwiched complex anti–cancer-protective membrane has been used as a suitable anti–cancer-protective membrane for the treatment of polyaromatic hydrocarbon compounds.

Experimental methods, techniques and materials

Materials

Powder of Cadmium (99.99%), Sulfuric acid (98%), Sodium nitrate (30%), Hydrogen peroxide (H_2O_2) (30%), Potassium permanganate ($KMnO_4$) and DI water for synthesizing Cadmium Oxide (CdO) were purchased from Sigma–Aldrich Corporation. Tetra Butyl Titanate (TBT), Acetic acid (HAc) and stainless steel autoclave for synthesizing CdO microsphere were also purchased from Sigma–Aldrich Corporation. Polyether Ether Ketone (PEEK) Merck Company, Tetrahydrofuran (THF) as solvents, Polysorbate 80 as the surfactant, PEEK as a pore former, TBA, which has been listed among the USA EPA priority pollutant, was purchased from Sigma–Aldrich Corporation.

Preparation of cadmium oxide (CdO)–DNA/RNA sandwiched complex

Cadmium Oxide (CdO) was prepared from natural Cadmium (Cd) powder according to the different methods and techniques [1, 2] and the many procedures which described with some modifications previously [1, 2]. Briefly, 10 (gr) of Cadmium (Cd) was added into 150 (ml) of Sulfuric acid (98%) while syringed at room temperature for 96 h period. Then, 550 (mg) of Sodium nitrate was added in to the mixture and stirred for 12 h. The dispersion was cooled by ice bath. Next, 85 (gr) of $KMnO_4$ was slowly added to the mixture during 90 (min). Afterward, the mixture of temperature was kept to 20–30 °C while it was stirring for another 6 h. The ice bath was removed after 6 h. The reaction was followed by adding 250 (ml) of DI water in to the dispersion during 90 (min). Finally, an aqueous solution of H_2O_2 was added to the dispersion. We could have washed DNA/RNA with aqueous HCl until no sulfite ions were found. The pH of the solution was remained at 6. Next, the synthesized DNA/RNA was dried at 60 °C for 72 h.

Preparation of thin layers of cadmium oxide (CdO) plasmonic nanostructure

Typically, 10 (ml) of Tetra Butyl Titanate (TBT) was added drop wisely to 150 (ml) of HAc with stirring for 75 (min). After that, the white suspension was obtained. It could transfer to Teflon stainless–steel autoclave. It was heated at 330 °C for 24 h. The product was washed by DI water and ethanol. The material was dried at 110 °C for 60 h and, after that, calcined at 840 °C for 5 h. It was obtained thin layers of CdO plasmonic nanostructure.

DNA/RNA–CdO sandwiched complex synthesis

DNA/RNA–CdO sandwiched complex was prepared according to the previous reports [1, 2]. 75 (mg) of CdO was well dissolved in to 550 (ml) of DI water and then, 840 (mg) of layers of CdO plasmonic nanostructure was added to the above solution. After that, it was kept under ultrasonic conditions for 20 h. Then, it was kept under stirring for 15 h. Finally, the mixture was centrifuged and dried for 10 h. Molecular structure of DNA/RNA–CdO sandwiched complex and also DAN/RNA–CdO in a human cancer cell are illustrated in fig. 1 and 2, respectively.

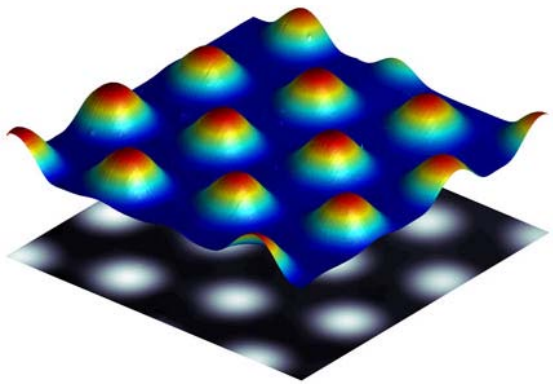

Fig. 1: Molecular structure of DNA/RNA–CdO sandwiched complex

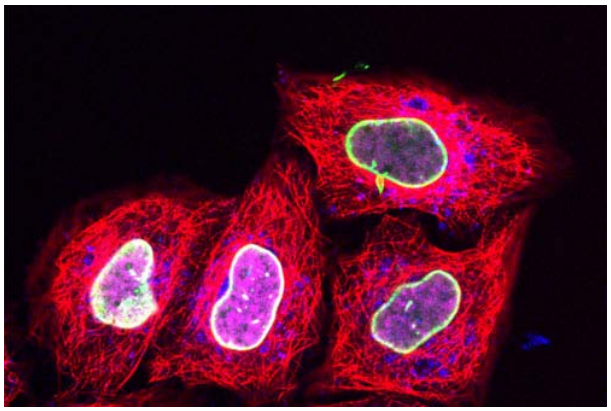

Fig. 2: Molecular structure of DNA/RNA–CdO sandwiched complex

Anti–cancer properties

The overall porosity of an anti–cancer-protective membrane (ε) can be calculated using the gravimetric method as presented in the Eq. (1):

$$\varepsilon = \frac{\omega_1 - \omega_2}{A \times L \times d_w} \quad \text{..... (1)}$$

Where ω_1 and ω_2 are the wet and dry weights of the anti–cancer-protective membrane, respectively. *dw* is the water density (0.998 gr(cm)$^{-3}$), *A* is the effective area of the anti–cancer protective membrane, a circular anti–cancer protective membrane piece of weighed (W_d) after vacuum drying for 96 h at 50 °C. Then, the anti–cancer protective membrane was immersed in DI water, overnight and weighed (W_W) after the surface was blotted with a filter paper, and the mean pore radius of the anti–cancer protective membrane (r_m) can be calculated using the Guerout–Elford–Ferry Equation (Eq. (2)):

$$r_m = \sqrt{\frac{(2.9 - 1.75\varepsilon) \times 8\eta l Q}{\varepsilon \times A \times \Delta P}} \quad \text{..... (2)}$$

η is the water viscosity (8.9×10^{-4} pas), ΔP is the operation pressure (1 bar), *Q* is the permeated pure water amount (m^3/s), *l* is the anti–cancer-protective membrane thickness (m) and *A* is the surface area (m^2) [1, 2].

Anticancer experiment

The surfactants enhanced the solubilization of Hydrophobic Organic Compounds (HOCs) by decreasing the interfacial tension between the contaminants and water [1, 2]. 50 (ml) of Polysorbate 80 were placed in 200 (ml) flask. Then, TBA was added to the flask more than the required amount to saturate solution. The flask was put on a shaker (1000 rpm, at 27 °C) for 72 h and then the sample was centrifuged at 10000 (rpm) for 90 (min) to completely un–dissolve the solute. Afterward, the concentration of suspension was determined by UV–Vis spectroscopy [1, 2].

Plasmonic properties

The anti–cancer-protective membrane was first evaluated with pure water flux before using TBA solution. All the anti–cancer-protective membranes have an effective area 23.273 (cm^2) and each was pressurized at 5 (bar) for the period of 45 (min). In order to achieve steady-state flux. Pure water flux of anti–cancer-protective membrane (JW_1), which was evaluated at 5 (bar) could be calculated using Eq. (3):

$$J_{W1} = \frac{V}{A \times t \times \Delta P} \quad \text{..... (3)}$$

Where *V* is the volume of permeate pure water (*L*), *A* is the anti–cancer-protective membrane effective area in (cm^2), *t* is permeation flux time (*h*) and ΔP is the pressure (bar) are used. To determine rejection of anti–cancer-protective membrane against crude oil and egg albumin or Bovine Serum Albumin (BSA) the following Equation can be used (Eq. (4)) [1, 2]:

$$R\% = \left(1 - \frac{C_P}{C_F}\right) \times 100 \quad \text{..... (4)}$$

Where C_P and C_F are the concentration of TBA in permeate and feed (mg/l), respectively. The UV–Vis irradiation was used to determine the TBA concentration. In order to obtain Flux Recovery Rate (FRR) of the anti–cancer-protective membrane, the feed solution tank was refilled with DI water. The pure water flux (JW_2) was evaluated to obtain FRR% using Eq. (5) [1, 2]:

$$FRR = \frac{J_{W_2}}{J_{W_1}} \times 100 \quad \text{..... (5)}$$

The higher value of FRR, the better antifouling property of the anti–cancer protective membrane [1, 2]. Fouling occurs due to the filtration of cake/gel layer on the anti–cancer-protective membrane surface. The accumulation of foulants onto the anti–cancer-protective membrane pore acts as a driving force for the diffusion of hydrophobic molecules through the anti–cancer-protective membrane structure, negatively affecting to both the water permeation and the rejection potential of anti–cancer-protective membranes.

Anti–cancer-protective membrane

The total fouling resistance of the polymeric anti–cancer-protective membrane (R_T) is calculated from r_r and r_{ir}. r_r is a reversible fouling ratio which describes the fouling caused by concentration polarization, r_{ir} is an irreversible fouling ratio which describes the fouling caused by adsorption or deposition of protein molecules on the anti–cancer-protective membrane surface (Eqs. (6) and (7)):

$$r_r = \frac{J_{W_2} - J_P}{J_{W_1}} \quad \text{..... (6)}$$

$$r_{ir} = \frac{J_{W_1} - J_{W_2}}{J_{W_1}} \quad \text{..... (7)}$$

R_t is the sum of r_r and r_{ir}, J_{W1} is the permeation water flux (kg/m^{2}h) (Eq. (8)):

$$J_{W_1} = \frac{M}{At} \quad \text{..... (8)}$$

Where *M* is the weight of collected permeate flux, *A* is the anti–cancer-protective membrane effective area, *t* is the permeation time, J_{W2} is the water flux cleaned anti–cancer-protective membrane and J_P is the flux of the BSA solution (Eq. (9)) [1, 2]:

$$R_t = \left(1 - \frac{J_P}{J_{W1}}\right) \times 100 \quad \text{..... (9)}$$

Under special pressure, after the pure water test, the BSA solutions are immediately replaced in the filtration cell for 360 (min) [1, 2].

Anti–cancer-protective membrane preparation

To prepare Alireza Heidari Solution, which shows that sonicated at 150 °C for 90 (min) and then dried PEEK polymer. Pellets were added in to the mixture dispersed sufficiently well by stirring until the homogenous suspension was obtained. Then, the solution was remained to room temperature for degassing of solution due to 96 h. To prepare Mixed Matrix Membrane (MMM), the prepared uniform suspension was poured in to the glass-smooth plate and cast by a casting blade. Then, the glass plate was immersed in to the deionized water at room temperatures for 96 h to remove solvent and solidify the anti–cancer-protective membrane as shown in fig. 3. The anti–cancer-protective membrane thickness was 850 (nm). Addition of 0.55 (gr) nanoparticles to the solution is not suitable, the viscosities of the solution was very high.

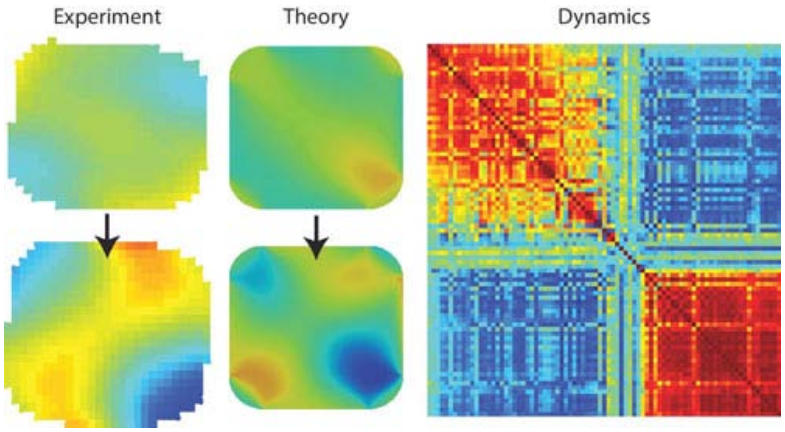

Fig. 3: The glass plate was immersed in to the deionized water at room temperatures for 96 (h) to remove solvent and solidify the anti–cancer-protective membrane

Characterizations

The structure of DNA/RNA–CdO sandwiched complex were examined by X–Ray Diffraction (XRD), with monochrome Cu Ka radiation. XRD was operated at 85 (KV), 65 (mA). Attenuated Total Reflection–Fourier Transform–Infrared (ATR–FTIR) spectroscopy was used to detect the chemical composition of DNA/RNA–CdO sandwiched complex. All samples were recorded in the wavenumber of 4000–400 (cm^{-1}). Raman spectroscopy is an excellent method to characterize nanomaterials. Energy–Dispersive X–Ray spectroscopy (EDAX) was used to quantify the element content of DNA/RNA–CdO sandwiched complex on the surface of best anti–cancer-protective membrane. Transmission Electron Microscopy (TEM), the characterization of synthesized DNA/RNA–CdO sandwiched complex were analyzed by TEM. The DNA/RNA–CdO sandwiched complex anti–cancer-protective membrane was dispersed in alcohol. The solution was sonificated for 75 min to produce homogenous solution. The suspension was dried in vacuum oven at 135 °C. 3D–Atomic–Force Microscopy (3D–AFM) the surface structure and the surface roughness of all anti–cancer-protective membranes were measured. The scan was made over an area of 85 (μm) × 10 (μm) to obtain surface roughness and pore size by tapping mode at 135 °C. The top surface and cross-section of anti–cancer-protective membranes were characterized by SEM; the sample was prepared by fracturing the anti–cancer-protective membranes in liquid Nitrogen so that the anti–cancer-protective membrane was sharply cut. The sample of anti–cancer protective membrane sputters with Gold. Contact angle, using the sessile drop method with a goniometer, hydrophilicity of each anti–cancer protective membrane was measured at 135 °C, 75% humidity. 1 (μl) of DI water was carefully dropped on the top surface of anti–cancer-protective membrane. The contact angle was equipped with video capture at room temperature. The angle between of water and anti–cancer-protective membrane was determined after ten times.

Solving scalar abraham–lorentz–dirac–langevin (aldl) equation for interaction between thin layers of cadmium oxide (cdo) plasmonic nanostructure and synchrotron radiation

We give a first principles' derivation of the ALDL equation, which depicts the quantum expectation value for a particle's trajectory and its stochastic fluctuations by combining the worldline path integral quantization with the Feynman–Vernon influence functional or closed–time–path effective action methods. At the lowest order, the equations of motion are approximated by a stochastic Lorentz–Dirac equation.

Mathematically, the ALDL force is given in SI units by:

$$F_{rad} = \frac{\mu_0 q^2}{6\pi c} \dddot{\mathbf{r}} = \frac{q^2}{6\pi\varepsilon_0 c^3} \dddot{\mathbf{r}} \quad \text{..... (10)}$$

or in Gaussian units by:

$$F_{rad} = \frac{2}{3}\frac{q^2}{c^3} \dddot{\mathbf{r}} \quad \text{..... (11)}$$

Here F_{rad} is the force, $\dddot{\mathbf{r}}$ is the derivative of acceleration, or the third derivative of displacement), also called jerk, μ_0 is the magnetic constant, ε_0 is the electric constant, c is the speed of light in free space, and q is the electric charge of the particle.

Note that this formula is for non–relativistic velocities; Dirac simply renormalized the mass of the particle in the equation of motion to find the relativistic version (below).

Physically, an accelerating charge emits radiation (according to the Larmor formula), which carries momentum away from the charge. Since momentum is conserved, the charge is pushed in the direction opposite the direction of the emitted radiation. In fact, the formula above for radiation force can be derived from the Larmor formula, as shown below.

The simplest derivation for the self–force is found for periodic motion from the Larmor formula for the power radiated from a point charge:

$$P = \frac{\mu_0 q^2}{6\pi c} a^2 \quad \text{..... (12)}$$

If we assume the motion of a charged particle is periodic, then the average work done on the particle by the ALDL force is the negative of the Larmor power integrated over one period from τ_1 to τ_2:

$$\int_{\tau_1}^{\tau_2} F_{rad} \cdot v dt = \int_{\tau_1}^{\tau_2} -P dt = -\int_{\tau_1}^{\tau_2} \frac{\mu_0 q^2}{6\pi c} a^2 dt = -\int_{\tau_1}^{\tau_2} \frac{\mu_0 q^2}{6\pi c} \frac{dv}{dt} \cdot \frac{dv}{dt} dt \quad \text{..... (13)}$$

The above expression can be integrated by parts. If we assume that there is periodic motion, the boundary term in the integral by parts disappears:

$$\int_{\tau_1}^{\tau_2} F_{rad} \cdot v dt = -\frac{\mu_0 q^2}{6\pi c} \frac{dv}{dt} \cdot v \Big|_{\tau_1}^{\tau_2} + \int_{\tau_1}^{\tau_2} \frac{\mu_0 q^2}{6\pi c} \frac{d^2 v}{dt^2} \cdot v dt = -0 + \int_{\tau_1}^{\tau_2} \frac{\mu_0 q^2}{6\pi c} \dot{a} \cdot v dt \quad \text{..... (14)}$$

Clearly, we can identify:

$$F_{rad} = \frac{\mu_0 q^2}{6\pi c} \dot{a} \quad \text{..... (15)}$$

A more rigorous derivation, which does not require periodic motion, was found using an Effective Field Theory formulation. An alternative derivation, finding the fully relativistic expression, was found by Dirac.

Below is an illustration of how a classical analysis can lead to surprising results. The classical theory can be seen to challenge standard pictures of causality, thus signaling either a breakdown or a need for extension of the theory. In this case, the extension is to quantum mechanics and its relativistic counterpart quantum field theory. See the quote from Rohrlich in the introduction concerning "the importance of obeying the validity limits of a physical theory".

For a particle in an external force F_{ext}, we have:

$$m\dot{v} = F_{rad} + F_{ext} = mt_0 \ddot{v} + F_{ext} \quad \text{..... (16)}$$

Where

$$t_0 = \frac{\mu_0 q^2}{6\pi mc} \quad \text{..... (17)}$$

This equation can be integrated once to obtain:

$$m\dot{v} = \frac{1}{t_0} \int_t^{\infty} \exp\left(-\frac{t'-t}{t_0}\right) F_{ext}(t') dt' \quad \text{..... (18)}$$

The integral extends from the present to infinitely far in the future. Thus, future values of the force affect the acceleration of the particle in the present. The future values are weighted by the factor:

$$\exp\left(-\frac{t'-t}{t_0}\right) \quad \text{..... (19)}$$

Which falls off rapidly for times greater than t_0 in the future. Therefore, signals from an interval approximately t_0 into the future affect the acceleration in the present. For an electron, this time is approximately 10^{-24} sec, which is the time it takes for a light wave to travel across the "size" of an electron, the classical electron radius. One way to define this "size" is as follows: It is (up to some constant factor) the distance r such that two electrons placed at rest at a distance r apart and allowed to fly apart, would have sufficient energy to reach half the speed of light. In other words, it forms the length (or time, or energy) scale where something as light as an electron would be fully relativistic. It is worth noting that this expression does not involve Planck's constant at all, so although it indicates something is wrong at this length scale, it does not directly relate to quantum uncertainty or to the frequency–energy relation of a photon. Although it is common in quantum mechanics to treat $\hbar \to 0$ as a "classical limit", some speculate that even the classical theory needs renormalization, no matter how Planck's constant would be fixed.

To find the relativistic generalization, Dirac renormalized the mass in the equation of motion with the ALDL force in 1938. This renormalized equation of motion is called the ALDL equation of motion.

The expression derived by Dirac is given in signature $(-,+,+,+)$ by:

$$F_{\mu}^{rad} = \frac{\mu_0 q^2}{6\pi mc} \left[\frac{d^2 p_{\mu}}{d\tau^2} - \frac{p_{\mu}}{m^2 c^2} \left(\frac{dp_{\nu}}{d\tau} \frac{dp^{\nu}}{d\tau} \right) \right] \quad \text{..... (20)}$$

With Liénard's relativistic generalization of Larmor's formula in the co–moving frame,

$$P = \frac{\mu_0 q^2 \alpha^2 \gamma^6}{6\pi c} \quad \text{..... (21)}$$

One can show this to be a valid force by manipulating the time average equation for power:

$$\frac{1}{\Delta t}\int_0^t P dt = \frac{1}{\Delta t}\int_0^t F.v dt \quad \text{..... (22)}$$

Similar to the non–relativistic case, there are pathological solutions using the ALDL equation that anticipate a change in the external force and according to which the particle accelerates in advance of the application of a force, so-called preacceleration solutions. One resolution of this problem was discussed by Yaghjian, and is further discussed by Rohrlich and Medina.

RESULTS AND DISCUSSION

Analysis of ART–FTIR, Raman, XRD and EDAX spectra

Fig. 4 illustrates the ATR–FTIR spectrum of DNA/RNA–CdO sandwiched complex. In order to obtain the information about the functional group of DNA/RNA–CdO sandwiched complex, the ATR–FTIR spectrum of DNA/RNA–CdO sandwiched complex materials were measured and shown in fig. (4). It was clear that DNA/RNA–CdO sandwiched complex showed many absorption peaks that correspond to various Oxygen functional groups, such as carboxylates or ketones C=O stretching (1777 cm^{-1}), water O–H bending and C≡C stretching (1727 cm^{-1}), C–O stretching (1284 cm^{-1}), C–O stretching of ether group (1227 cm^{-1}) and C–O stretching of epoxide (999 cm^{-1}) [1, 2]. As for the DNA/RNA–CdO sandwiched complex composite prepared through hydrothermal reaction, the spectrum showed a low absorption–peak intensity of the Oxygen functional groups at 1000–2000 (cm^{-1}) compared to that of DNA/RNA–CdO sandwiched complex. Especially for the peak at 1885 (cm^{-1}) (C=O) of DNA/RNA–CdO sandwiched complex composite; the peak intensity decreased greatly compared to that of DNA/RNA–CdO sandwiched complex. However, the strong peaks at 400–1400 (cm^{-1}) of DNA/RNA–CdO sandwiched complex composite were attributed to the stretching vibration of Cd–O–Cd or Cd–O–DNA/RNA [1, 2]. Therefore, the above results confirmed that the formation of DNA/RNA–CdO sandwiched complex composite and chemical interaction strong between surface hydroxyl groups of CdO and functional groups of DNA/RNA.

XRD patterns of DNA/RNA, CdO microsphere and DNA/RNA–CdO sandwiched complex are shown in fig. 5. The strong peak of DNA/RNA at 2θ angle around 27° can be attributed to the reaction between CdO and DNA/RNA sheet in the range of 10°–120°. The diffraction peak at 2θ of 15°, 25°, 35°, 45°, 55°, 65°, 75° and 85° are attributed to DNA/RNA–CdO sandwiched complex. DNA/RNA–CdO sandwiched complex shows similar peaks with DNA/RNA–CdO sandwiched complex [1, 2]. Fig. 5 shows XRD of DNA/RNA–CdO sandwiched complex at one graph. Raman spectroscopy is one of the most widely used techniques to provide the structural and electronic properties of CdO–based materials.

Raman spectra of DNA/RNA–CdO sandwiched complex were recorded and shown as fig. 6. The typical four peaks of DNA/RNA–CdO sandwiched complex at 222 (cm^{-1}), 405 (cm^{-1}), 518 (cm^{-1}) and 620 (cm^{-1}) were observed compared with that of DNA/RNA–CdO sandwiched complex, which was ascribed to DNA/RNA–CdO sandwiched complex [1, 2]. The strong bands occurred at around 1184 (cm^{-1}) (G band) and 1427 (cm^{-1}) (D band) in DNA/RNA–CdO sandwiched complex composite. The D and G band is a common feature for sp^3 and sp^2 in-plane vibrations of bonded Carbons [1, 2]. The intensity ratio of the D band to the G band usually reflects the order of defects in DNA/RNA–CdO sandwiched complex. The calculated D/G intensity ratios of DNA/RNA–CdO sandwiched complex composite were 0.1123 and *0.4327*, respectively. These results agreed well with the results of Alireza Heidari group [1, 2]. Moreover, shape, intensity and position of the 2D band of DNA/RNA in the DNA/RNA–CdO sandwiched complex composite can indicate that the single and multilayer properties of the DNA/RNA sheet [1, 2]. From the Raman spectra of DNA/RNA–CdO sandwiched complex composite, we can see that the 2D peak is located at 3150 (cm^{-1}), which shifted to the high wavenumber region compared to that of single-layer DNA/RNA–CdO sandwiched complex (2888 cm−1). We can also see that the peak shape of DNA/RNA in DNA/RNA–CdO sandwiched complex composite is asymmetric compared to a symmetric 2D band of single-layer DNA/RNA–CdO sandwiched complex, which indicated that the prepared DNA/RNA–CdO sandwiched complex in the composites was multilayer. In addition, the G band of DNA/RNA–CdO sandwiched complex is situated at 1774 (cm^{-1}), which shifted to high wavenumber region compared to that of single-layer DNA/RNA–CdO sandwiched complex (1660) (cm^{-1}). These results also indicated that the DNA/RNA in the single-layer DNA/RNA–CdO sandwiched complex composite was multilayer. These results are consistent with the TEM observation (will be explained later in fig. 11.

However, the ratio of intensity of D/G bands is a measure of the defects present on DNA/RNA–CdO sandwiched complex structure. The DNA/RNA–CdO sandwiched complex band is a result of in-plane vibrations of sp^2 bonded Cadmium atoms, whereas the D band is due to out-of-plane vibrations attributed to the presence of structural defects. Now, when we compare the spectra of DNA/RNA–CdO sandwiched complex together, DNA/RNA–CdO sandwiched complex will have a higher D band. This is due to the disruption of sp^2 bonds of the Cadmium as DNA/RNA–CdO sandwiched complex has oxidative functional groups.

Therefore, if the D band is higher, it means that the sp^2 bonds are broken, which in turn means that there are more sp^3 bonds. However, D band can be present due to various other reasons. Therefore, if D/G ratio in DNA/RNA–CdO sandwiched complex is higher than DNA/RNA, it means that there are defects. It does not mean that we have more sp^3 than sp^2 in the same sample. In fact, it shows that we have more sp^3 in DNA/RNA–CdO sandwiched complex compared to DNA/RNA.

EDAX of the modified anti–cancer-protective membrane is shown in fig. 7 presence of elements on the anti–cancer-protective membrane such as Cadmium (Cd), Oxygen (O) and Nitrogen (N). The results show confirms the successful incorporation of DNA/RNA–CdO sandwiched complex in the Mixed Matrix Membrane (MMM).

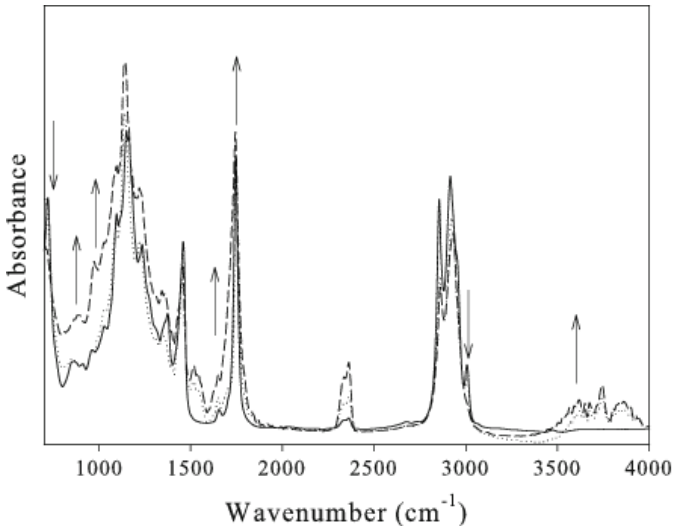

Fig. 4: Attenuated total reflection–fourier transform–infrared (ATR–FTIR) spectrums of (a) DNA–CdO (continuous line) and (b) RNA–CdO (dashed line) sandwiched complexes

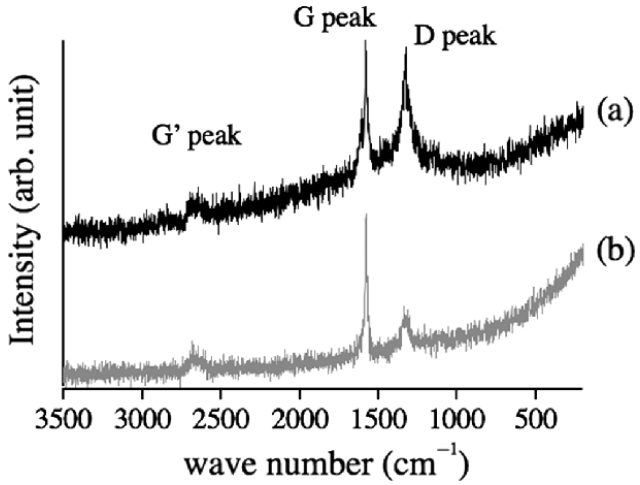

Fig. 5: XRD spectrums of (a) DNA–CdO and (b) RNA–CdO sandwiched complexes

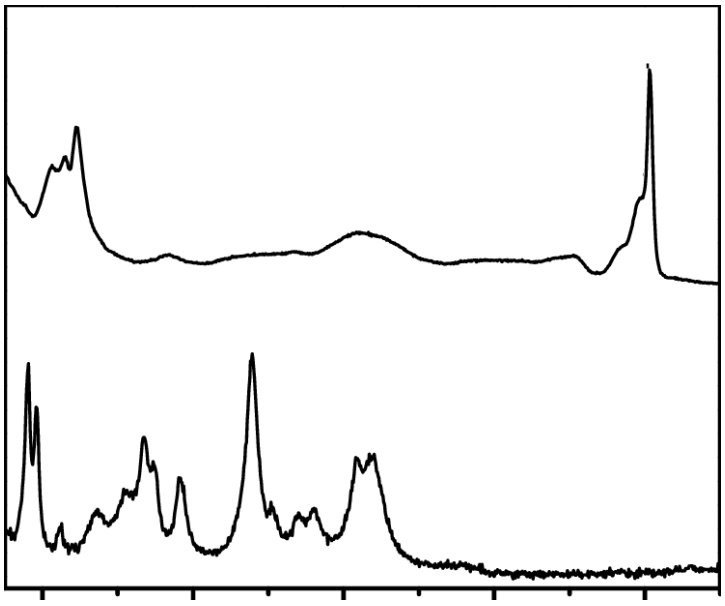

Fig. 6: Raman spectrums of (a) DNA–CdO (upper) and (b) RNA–CdO (lower) sandwiched complexes

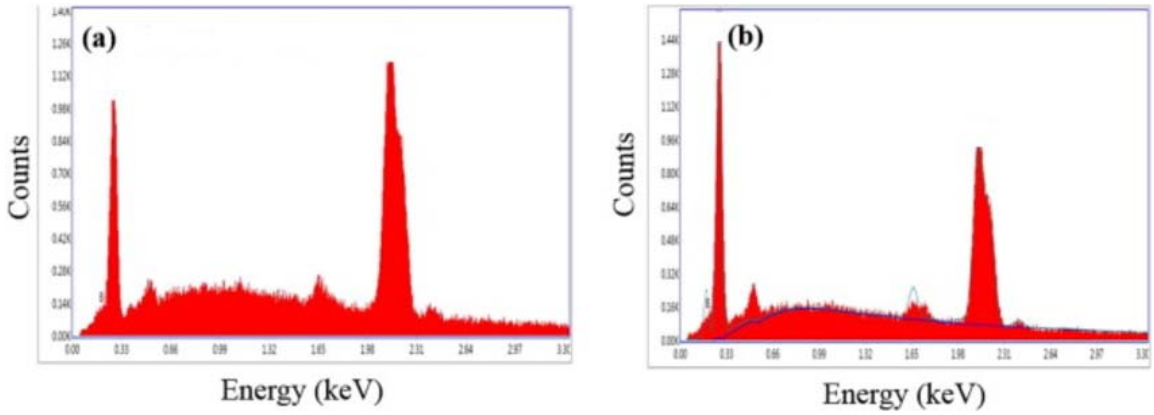

Fig. 7: EDAX spectrums of (a) DNA–CdO and (b) RNA–CdO sandwiched complexes

Analysis of SEM, TEM and 3D–AFM images

The surface morphologies of the PEEK anti–cancer-protective membranes and the thicknesses of the selective layers were determined by SEM. The images of surface area of anti–cancer-protective membrane are shown in fig. 8. The top surface of anti–cancer-protective membrane shows the size of pore decreases when loading of DNA/RNA–CdO sandwiched complexes increases at Mixed Matrix Membrane (MMM). However, by loading of DNA/RNA–CdO sandwiched complexes on the anti–cancer-protective membrane, hydrophilicity of anti–cancer-protective membrane increases which also indicated by contact angle results [1, 2]. The hydrophilicity and the pore size of anti–cancer-protective membrane play important roles on separation. Cell membranes with their selective permeability play important functions in the tight control of molecular exchanges between the cytosol and the extracellular environment as the intracellular membranes do within the internal compartments. For this reason, the plasma membranes often represent a challenging obstacle to the intracellular delivery of many anti-cancer molecules. The active transport of drugs through such barrier often requires specific carriers able to cross the lipid bilayer. Cell-penetrating peptides (CPPs) are generally 5–30 amino acids long which, for their ability to cross cell membranes, are widely used to deliver proteins, plasmid DNA, RNA, oligonucleotides, liposomes and anti-cancer drugs inside the cells. In this review, we describe the several types of CPPs, the chemical modifications to improve their cellular uptake, the different mechanisms to cross cell membranes and their biological properties upon conjugation with specific molecules. Special emphasis has been given to those with promising applications in cancer therapy. The asymmetric anti–cancer-protective membrane is ideal for obtaining high permeability, good hydrophilicity and excellent chemical resistance to the feed solution. The cross-section of modified anti–cancer-protective membrane shows an asymmetric structure. When the MMM is divided to three parts, top surface of anti–cancer-protective membrane shows the decrease of the pore size anti–cancer-protective membrane compares to the intermediate and bottom. At the bottom of anti–cancer-protective membrane, very large pore size is existed compare to the intermediate.

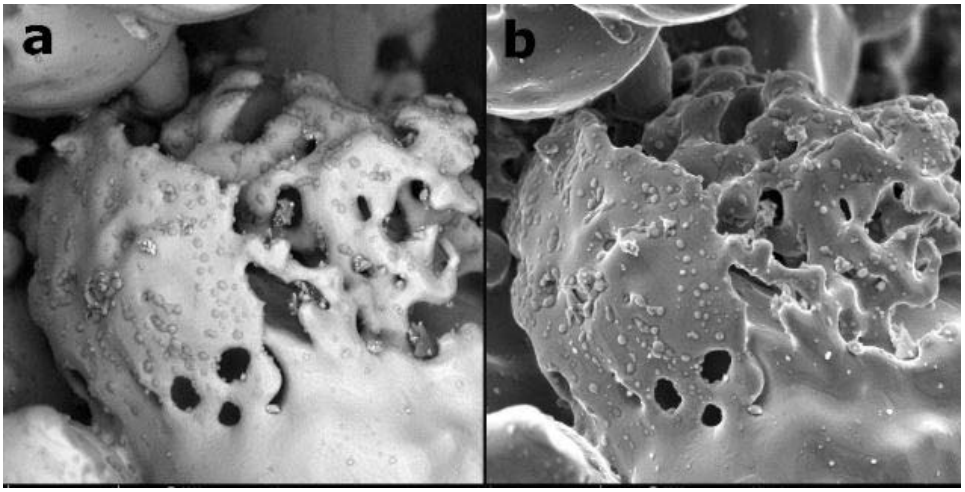

Fig. 8: SEM images of (a) DNA–CdO and (b) RNA–CdO sandwiched complexes

By increasing nanoparticles, the surface roughness of anti–cancer-protective membrane increases and the pore size decreases. The valley and the edges surface MMM become oriented with an increase in DNA/RNA–CdO sandwiched complexes nanoparticles and casting bar movement as shown in fig. 9 and 10. These roughness characteristics can strongly affect the adsorption/desorption of foulants on the anti–cancer-protective membrane surface and control the anti–cancer-protective membrane fouling. Accordingly, by decreasing the surface roughness of a hydrophilic anti–cancer protective membrane, the trapping of contaminants into the valleys and adhesion at peaks is restricted. The surface of the bare PEEK anti–cancer protective membrane has the lowest roughness and the roughness parameters are increased by the addition of DNA/RNA–CdO sandwiched complexes. Fig. 11 shows the nanohybride of DNA/RNA–CdO sandwiched complexes imbedded on polymer PEEK.

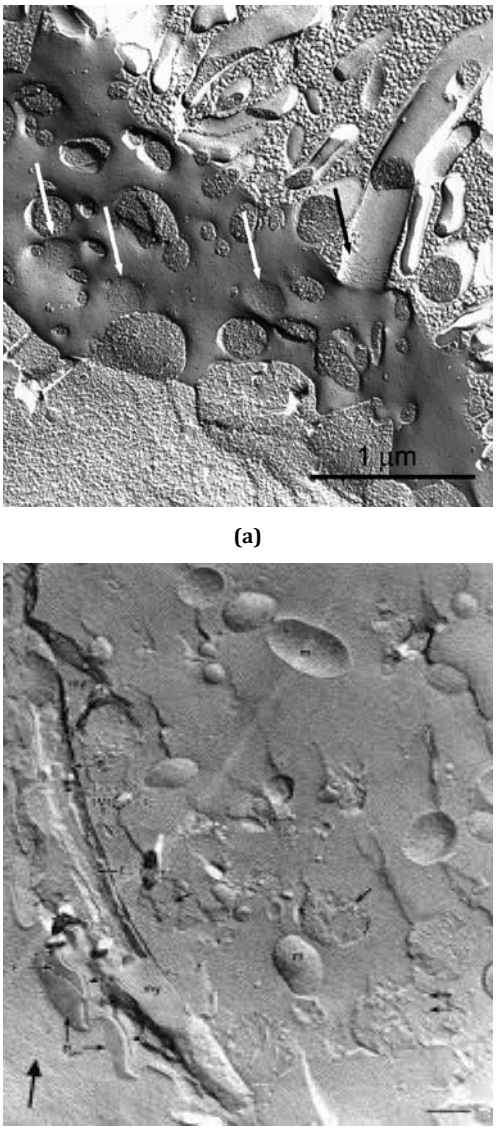

(a)

(b)

Fig. 9: TEM images of (a) DNA–CdO and (b) RNA–CdO sandwiched complexes

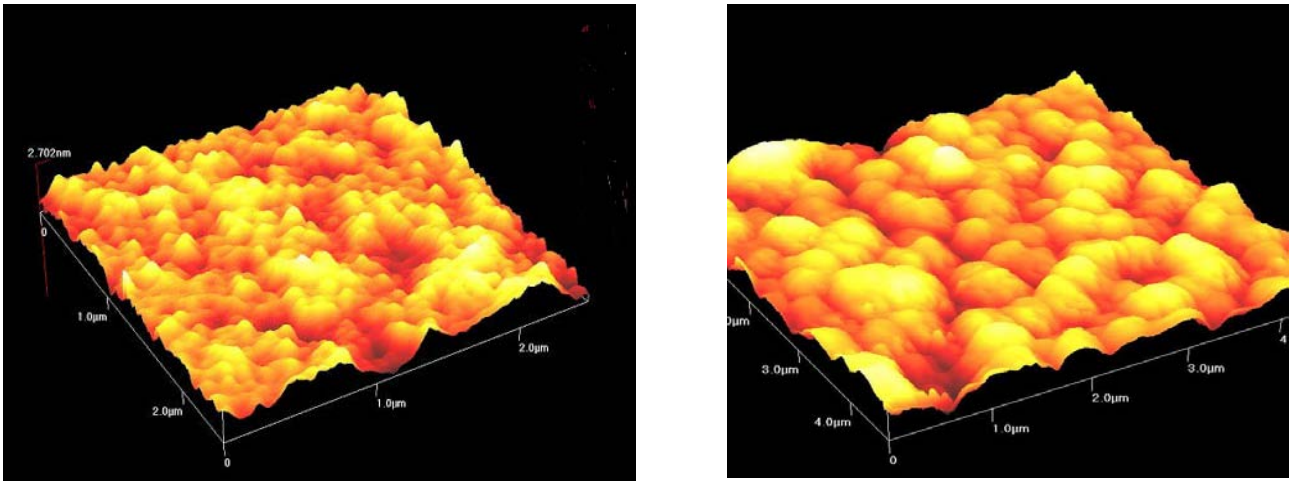

(a) **(b)**

Fig. 10: 3D–AFM images of (a) DNA–CdO and (b) RNA–CdO sandwiched complexes

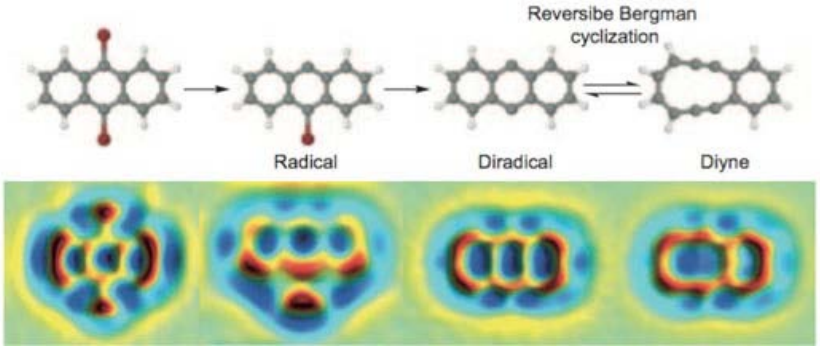

Fig. 11: Schematic and illustration of the nanohybride of DNA/RNA–CdO sandwiched complexes imbedded on polymer PEEK

Experiment for ultra-anti–cancer-protective filtration (UACPF)

Effect of different loading DNA/RNA–CdO sandwiched complex on cancer cells

Fig. 12 and 13 show permeation flux and rejection of all the anti–cancer-protective membrane as a function of operation time for cross-flow containing 25 (mg/l) and 85 (mg/l) PEEK, respectively. The best rejection of PEEK was occurred for 0.09 Wt% DNA/RNA–CdO sandwiched complex. The hybrid anti–cancer-protective membrane exhibits higher flux and higher rejection than neat PEEK anti–cancer-protective membrane. The main reason for the highest hydrophobicity of anti–cancer-protective membrane as expressed by the lowest contact angle. Among of all anti–cancer-protective membrane PEEK neat exhibit the lowest permeation flux (89 L/m^2. h. bar) and 0.09 Wt% DNA/RNA–CdO sandwiched complex shows excellent permeation flux 227 (L/m^2. h. bar). The pores are gradually blocked by adsorption of TBA drop on anti–cancer-protective membrane wall, which the main cause of formed narrower channel at anti–cancer-protective membrane. Then, TBA rejection of PEEK neat anti–cancer protective membrane increases. A good anti–cancer-protective membrane should be capable of achieving close to 100% rejection. High rejections are usually accompanied by low permeation fluxes. During fabrication, anti–cancer-protective membrane formation process plays an important role and certain factors need proper attention in order to produce a good separation anti–cancer-protective membrane. There are several parameters which have been found out to affect the morphology and performance of the prepared anti–cancer protective membrane by phase separation method and technique. Due to the effects of polymer concentration in the casting solution, higher rejection was obtained with denser anti–cancer protective membranes which had thicker skin layers and this resulted in poorer water permeability. On the other hand, the thinner and more porous skin layer anti–cancer protective membranes provided higher water permeability but poorer rejection. According to the contact angle test [1, 2], increasing of nanoparticle weight percentage in anti–cancer protective membrane will increase anti–cancer protective membrane hydrophobicity and consequently, it will increase permeation flux. On the other hand, increasing of nanoparticle weight percentage in anti–cancer protective membrane will increase anti–cancer protective membrane porosity and consequently, it will increase rejection percentage in anti–cancer protective membrane [1, 2].

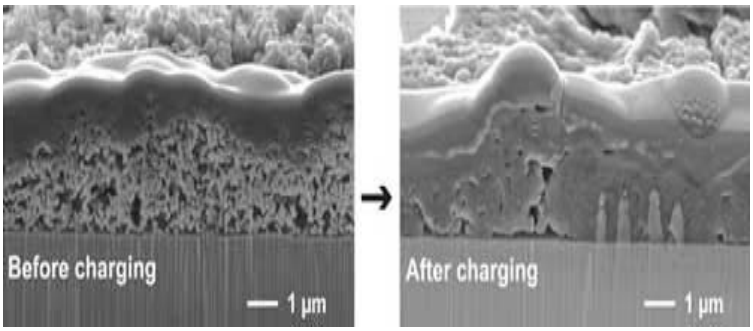

Fig. 12: Permeation flux and rejection of all the anti–cancer-protective membrane as a function of operation time for cross-flow containing 25 (mg/l) TBA

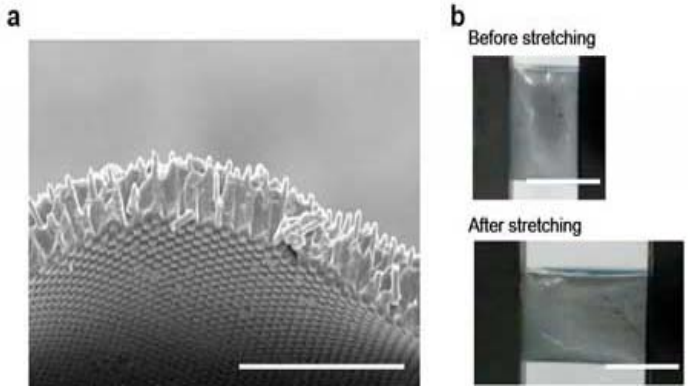

Fig. 13: Permeation flux and rejection of all the anti–cancer-protective membrane as function of operation time for cross-flow containing 65 (mg/l) TBA

Effect of triptycene barrelene anthracene (TBA) concentration on cancer cells

Fig. 14 shows sharply decreasing of permeation flux of (0.09 Wt% DNA/RNA–CdO sandwiched complex) anti–cancer-protective membrane when increasing concentration of TBA under 0.5 bar at 33 °C (from 15, 25, 35, 45, 55, 65, 75, 85 and 95 (mg/l)). The results showed that PEEK neat anti–cancer-protective membrane has more fouling anti–cancer-protective membrane. One of the possible reasons for decreasing of flux is the concentration of polarization on the surface of anti–cancer-protective membrane along the increase of TBA concentration which is the main reason to form gel layer on the anti–cancer protective membrane. Another reason for flux decline is pore-blocking owing to the impermeability of large drop of TBA.

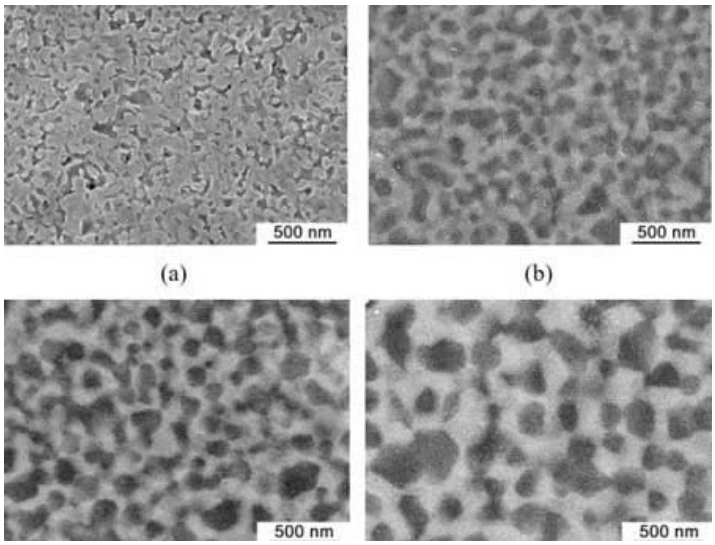

Fig. 14: Sharply decreasing of permeation flux of (0.09 Wt% DNA/RNA–CdO sandwiched complex) anti–cancer protective membrane when increasing concentration of TBA under 0.5 bar at 33 °C (from 15, 25, 35, 45, 55, 65, 75, 85 and 95 (mg/l))

Effect of trans–anti–cancer–protective membrane pressure (TACPMP) on cancer cells

Fig. 15 shows the effects of Trans–Anti–Cancer–Protective–Membrane Pressure (TACPMP) on the cancer cell. This suggests that when operating pressure gets too high, the anti–cancer-protective membrane will be blocked by droplet of pollutant. The formation of gel layer occurs immediately, which caused the flux to decline sharply. The anti–cancer-protective membrane pores at higher pressure leading to anti–cancer-protective membrane fouling at higher rate. These results are consistent with the previous reports [1, 2]. The Flux Recovery Rate (FRR) of (0.09 Wt% DNA/RNA–CdO sandwiched complex) decreases from 0.99% to 0.23% with increasing pressure from 1.7 to 2.9.

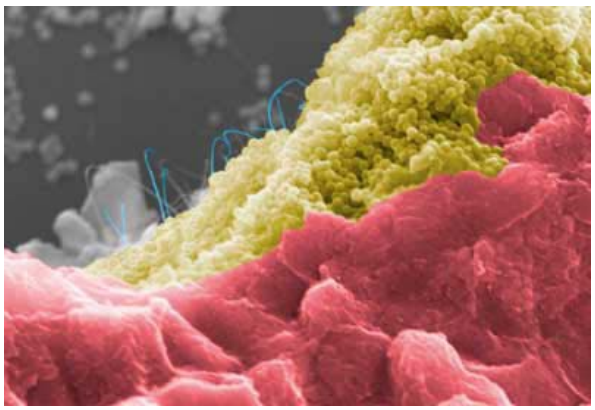

Fig. 15: Effects of trans–anti–cancer-protective–membrane pressure (TACPMP) on the cancer cell

Hydrophilicity of mixed matrix membrane (MMM) DNA/RNA–CdO sandwiched complex in cancer cells

Hydrophilicity of PEEK/DNA/RNA–CdO sandwiched complex of each anti–cancer-protective membrane measures by the contact angle. It is commonly accepted that by increasing the loading of the DNA/RNA–CdO sandwiched complex, the contact angle is decreased and hydrophilicity of anti–cancer-protective membrane is indicated higher. According to the reports of Alireza Heidari *et al.* [1, 2] the hydroxyl groups of nanoparticles are able to interact with water molecules through Hydrogen bonding and the van der Waals force, which leads to an increase in water permeability.

Anti–cancer-protective properties of mixed matrix membrane (MMM)

Anti–cancer-protective membrane fouling, as one of the main drawbacks of anti–cancer-protective membranes, has various disadvantages such as flux decline, increment of operation cost, maintenance costs and anti–cancer-protective membrane degradation. Anti–cancer-protective membrane fouling consists of reversible fouling and irreversible fouling, reversible protein or organic material adsorption cause to reversible fouling, which could be removed by hydraulic cleaning. On the contrary, irreversible fouling results of strong adsorption of molecule on the surface or entrapment of pores. The antifouling and anti-cancer properties of anti–cancer-protective membrane was calculated from Flux Recovery Ratio (FRR), total fouling rate (R_t), reversible fouling ratio (R_r) and irreversible fouling rate (R_{ir}). As shown in fig. 16, the R_t were 88, 73, 62% for hybrid anti–cancer-protective membrane (DNA/RNA–CdO sandwiched complex) while 59.63% for PEEK neat. The R_r of hybrid anti–cancer-protective membranes were decreased from 18, 14, 10 while 49.43 for neat PEEK. The results show hybrid anti–cancer-protective membranes had excellent antifouling and anti–cancer ability in PEEK which is possible to have a good application in antifouling for polyaromatic hydrocarbons.

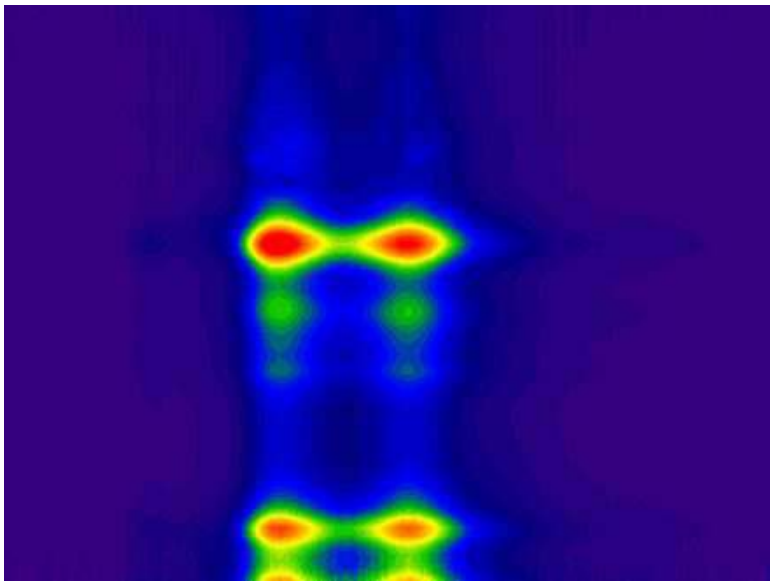

Fig. 16: Hybrid anti–cancer protective membranes such as DNA/RNA–CdO sandwiched complex possess possibility to have a good application in excellent antifouling and anti–cancer abilities and properties

CONCLUSION

In this study, PEEK ultrafiltration anti–cancer-protective membranes were prepared by phase inversion with adding different rate nanoparticles DNA/RNA–CdO sandwiched complex. It was used from surfactant Polysorbate 80 for increasing the solubility of TBA in water. The current study investigated effects of nanoparticles on permeate, hydrophilicity and antifouling of PEEK on the anti–cancer-protective membrane. Many reasons that make of DNA/RNA a suitable material to combine with CdO and used to make polymer anti–cancer-protective membrane. DNA/RNA provide a way to enhance the separation between the electron and the hole also increase the absorption range, including at the visible region. The new simple theoretical model of DNA/RNA for the interface exciton with an itinerant photo–excited hole is already studied. Finally, they also increase the interaction area and adsorption of pollutants and dyes with the photocatalyst by creating a π–π interaction. By increasing of DNA/RNA–CdO sandwiched complex nanohybrids increasing of hydrophilicity of MMM. The permeation flux of 100 (mg/l) PEEK was increased by increasing of the nanoparticles, which shows in anti–cancer-protective membrane contact angle test. Also, by increasing of the nanoparticles in anti–cancer-protective membrane increasing of roughness and decreasing of pore size of MMM. Therefore, the MMM (0.09 Wt %) with good rejection and low antifouling will be potentially useful for the treatment of the water pollutant with PAHs.

ACKNOWLEDGMENT

This study was supported by the Cancer Research Institute (CRI) Project of Scientific Instrument and Equipment Development, the National Natural Science Foundation of the United Sates, the International Joint BioSpectroscopy Core Research Laboratory Program supported by the California South University (CSU), and the Key project supported by the American International Standards Institute (AISI), Irvine, California, USA.

ABBREVIATION

CdO: Cadmium Oxide, TBA: Triptycene Barrelene Anthracene, PEEK: Polyether Ether Ketone, ATR–FTIR: Attenuated Total Reflection–Fourier Transform–Infrared, XRD: X–Ray Diffraction, SEM: Scanning Electron Microscope, EDAX: Energy–Dispersive X–Ray, 3D–AFM: 3D–Atomic–Force Microscopy, TEM: Transmission Electron Microscopy, NSO: Nitrogen Sulfuer Oxygen, PAHs: Polycyclic Aromatic Hydrocarbons, SSA: Specific Surface Area, PVDF: Polyvinylidinedifluride, PSF: Polysulfonefluride, PES: Polyethersulfone, HMO: Hydrous Manganese Dioxide, MMM: Mixed Matrix Membrane, HAc: Acetic Acid, TBT: Tetra Butyl Titanate, THF: Tetrahydrofuran, HOCs: Hydrophobic Organic Compounds, FRR: Flux Recovery Rate, BSA: Bovine Serum Albumin, CPPs: Cell-Penetrating Peptides, UACPF: Ultra Anti–Cancer Protective Filtration, CAP: Cold Atmospheric Plasmas, TACPMP: Trans–Anti–Cancer–Protective Membrane Pressure, CBLs: Concentration Boundary Layers, ALDL: Abraham–Lorentz–Dirac–Langevin

FUNDING

Nil

AUTHORS CONTRIBUTIONS

All the authors have contributed equally.

CONFLICT OF INTERESTS

Declared none

REFERENCES

1. Couvreur P, Louvard D. COVID-19 and drugs: pathophysiology and therapeutic approaches. C R Biol. 2021;344(1):27-42. doi: 10.5802/crbiol.38, PMID 34213847.
2. White M, Kingma P, Tecle T, Kacak N, Linders B, Heuser J, Crouch E, Hartshorn K. Multimerization of surfactant protein D, but not its collagen domain, is required for antiviral and opsonic activities related to influenza virus. J Immunol. 2008;181(11):7936-43. doi: 10.4049/jimmunol.181.11.7936, PMID 19017984.
3. Vanitha V, Vijayakumar S, Nilavukkarasi M, Punitha VN, Vidhya E, Praseetha PK. Heneicosane- A novel microbicidal bioactive alkane identified from plumbago zeylanica L. Ind Crops Prod. 2020;154. doi: 10.1016/j.indcrop.2020.112748. PMID 112748.
4. Turro NJ, Lei XG, Ananthapadmanabhan KP, Aronson M. Spectroscopic probe analysis of protein-surfactant interactions: the BSA/SDSsystem. Langmuir. 1995;11(7):2525-33. doi: 10.1021/la00007a035.
5. Otzen DE. Protein unfolding in detergents: effect of micelle structure, ionic strength, pH, and temperature. Biophys J. 2002;83(4):2219-30. doi: 10.1016/S0006-3495(02)73982-9, PMID 12324439.
6. Israelachvili JN. Contrasts between intermolecular, interparticle, and intersurface forces, book chapter. Intermol Surf Forces. 2011:205-22.
7. Itoo FA, MirInt JM, Skoglund S, Blomberg E, Wallinder IO, Grillo I, Pedersen JS, Bergström LM. A novel explanation for the enhanced colloidal stability of silver nanoparticles in the presence of an oppositely charged surfactant. Phys Chem Chem Phys. 2017;19(41):28037-43. doi: 10.1039/c7cp04662f, PMID 28994441.
8. Wong FWF, Ariff AB, Stuckey DC. Downstream protein separation by surfactant precipitation: a review. Crit Rev Biotechnol. 2018;38(1):31-46. doi: 10.1080/07388551.2017.1312266, PMID 28427287.
9. Itoo FA, Mir JM, Malik NA, Ali A. Density functional aspects and thermodynamic evaluation of sodium dodecyl sulphate in aqueous tartrazine. J King Saud Univ Sci. 2020;32(4):2505-12. doi: 10.1016/j.jksus.2020.04.009.
10. Mir JM, Itoo FA. Experimental-DFT interface of hydrogen bonding description of 1:10 methanol-water solution. J Mol Liq. 2017;247:1-5. doi: 10.1016/j.molliq.2017.09.094. molliq.2017.09.094.
11. GM P, Maanvizhi S. Fast track usa regulatory approval for drugs to treat emerging infectious diseases: fast track approval. Asian J Pharm Clin Res. 2021;14:1-4.
12. Mahmood Alabdali AY, Chinnappan S, Abd Razik BM, RM, Khalivulla SI HR, Samein LH. Impact of covid-19 on multiple body organ failure: a review. Int J App Pharm. 2021;13(5):54-9. doi: 10.22159/ijap.2021v13i5.42653.
13. Sundararajan. Insights into corona/coronavirus disease 2019 pandemic–opinion versus evidence. Asian J Pharm Clin Res. 2021;14:13-5.
14. Mir JM, Maurya RC. Nitric oxide as a therapeutic option for COVID-19 treatment: a concise perspective. New J Chem. 2021;45(4):1774-84. doi: 10.1039/D0NJ03823G.
15. https://www.nationalgeographicNationalgeographic.com/science/2020/04/factors-allow-viruses-infect-humans-coronavirus. [Last accessed on 10 May 2021].
16. Koonin EV, Senkevich TG, Dolja VV. The ancient virus world and evolution of cells. Biol Direct. 2006;1:29. doi: 10.1186/1745-6150-1-29, PMID 16984643.
17. McIntosh K, Halonen P, Ruuskanen O. Report of a workshop on respiratory viral infections: epidemiology, diagnosis, treatment, and prevention. Clin Infect Dis. 1993;16(1):151-64. doi: 10.1093/clinids/16.1.151, PMID 8383547.
18. Ada GL, Jones PD. The immune response to influenza infection. Curr Top Microbiol Immunol. 1986;128:1-54. doi: 10.1007/978-3-642-71272-2_1, PMID 3533447.
19. Wiley DC, Skehel JJ. The structure and function of the hemagglutinin membrane glycoprotein of influenza virus. Annu Rev Biochem. 1987;56:365-94. doi: 10.1146/annurev.bi.56.070187.002053. PMID 3304138.
20. Sturman LS, Ricard CS, Holmes KV. Conformational change of the coronavirus peplomer glycoprotein at pH 8.0 and 37 degrees C correlates with virus aggregation and virus-induced cell fusion. J Virol. 1990;64(6):3042-50. doi: 10.1128/JVI.64.6.3042-3050.1990, PMID 2159562.
21. Chepurnov AA, Bakulina LF, Dadaeva AA, Ustinova EN, Chepurnova TS, Baker JR. Inactivation of Ebola virus with a surfactant nanoemulsion. Acta Trop. 2003;87(3):315-20. doi: 10.1016/S0001-706X(03)00120-7, PMID 12875924.
22. Hiemstra PS. Epithelial antimicrobial peptides and proteins: their role in host defense and inflammation. Paediatr Respir Rev. 2001;2(4):306-10. doi: 10.1053/prrv.2001.0165, PMID 12052302.
23. Backer JA, Klinkenberg D, Wallinga J. Incubation period of 2019 novel coronavirus (2019-nCoV) infections among travellers from Wuhan, China, 20-28 January 2020. Euro Surveill. 2020;25(5):2020. doi: 10.2807/1560-7917.ES.2020.25.5.2000062, PMID 32046819.
24. Bitko V, Musiyenko A, Barik S. Viral infection of the lungs through the eye. J Virol. 2007;81(2):783-90. doi: 10.1128/JVI.01437-06, PMID 17050596.
25. Rothe C, Schunk M, Sothmann P, Bretzel G, Froeschl G, Wallrauch C, Zimmer T, Thiel V, Janke C, Guggemos W, Seilmaier M, Drosten C, Vollmar P, Zwirglmaier K, Zange S, Wolfel R, Hoelscher M. Transmission of 2019-nCoV infection from an asymptomatic contact in germany. N Engl J Med. 2020;382(10):970-1. doi: 10.1056/NEJMc2001468, PMID 32003551.
26. Zou L, Ruan F, Huang M, Liang L, Huang H, Hong Z, Yu J, Kang M, Song Y, Xia J, Guo Q, Song T, He J, Yen HL, Peiris M, Wu J. SARS-CoV-2 viral load in upper respiratory specimens of infected patients. N Engl J Med. 2020;382(12):1177-9. doi: 10.1056/NEJMc2001737, PMID 32074444.
27. Fukushi M, Yamashita M, Miyoshi-Akiyama T, Kubo S, Yamamoto K, Kudo K. Laninamiviroctanoate and artificial surfactant combination therapy significantly increases survival of mice infected with the lethal influenza H1N1 virus. PLOS ONE. 2012;7(8):e42419. doi: 10.1371/journal.pone.0042419. PMID 22879974.
28. Hsieh IN, De Luna X, White MR, Hartshorn KL. The role and molecular mechanism of action of surfactant protein D in innate host defense against influenza A virus. Front Immunol. 2018;9:1368. doi: 10.3389/fimmu.2018.01368, PMID 29951070.
29. Guttentag S, Foster CD. Update in surfactant therapy. NeoReviews. 2011;12(11):e625-34. doi: 10.1542/neo.12-11-e625.
30. Jeon GW. Surfactant preparations for preterm infants with respiratory distress syndrome: past, present, and future. Korean J Pediatr. 2019;62(5):155-61. doi: 10.3345/kjp.2018.07185, PMID 30744318.
31. Walther FJ, Gordon LM, Waring AJ. Advances in synthetic lung surfactant protein technology. Expert Rev Respir Med. 2019;13(6):499-501. doi: 10.1080/17476348.2019.1589372, PMID 30817233.
32. Bocking T, Johnson L, Singh A, Desai A, Aulakh GK, Singh B. Research article expression of surfactant protein-A and D, and CD9 in lungs of 1 and 30 day old foals. BMC Vet Res. 2021;17(1):236. doi: 10.1186/s12917-021-02943-5, PMID 34225699.
33. Hammad MA, Muller BW. Increasing drug solubility by means of bile salt–phosphatidylcholine-based mixed micelles. Eur J Pharm Biopharm. 1998;46(3):361-7. doi: 10.1016/s0939-6411(98)00037-x, PMID 9885310.
34. Li J, Wang X, Zhang T, Wang C, Huang Z, Luo X, Deng Y. A review on phospholipids and their main applications in drug delivery systems. Asian J Pharm Sci. 2015;10(2):81-98. doi: 10.1016/j.ajps.2014.09.004.

35. van Hoogevest P, Wendel A. The use of natural and synthetic phospholipids as pharmaceutical excipients. Eur J Lipid Sci Technol. 2014;116(9):1088-107. doi: 10.1002/ejlt.201400219, PMID 25400504.
36. Yang C, Wu T, Qi Y, Zhang Z. Recent advances in the application of vitamin E TPGS for drug delivery. Theranostics. 2018;8(2):464-85. doi: 10.7150/thno.22711, PMID 29290821.
37. Bhusari KP, Khedekar PB, Umathe SN, Bahekar RH, Raghu Ram Rao A. Synthesis of 8-bromo-9-substituted-1,3-benzothiazolo-[5,1-b]-1. 3, 4-triazoles and their nthelmintic activity, Indian J. Hetero Chem. 2000;9:275-8.
38. Bhusare SR, Pawar RP, Vibhute YB. Synthesis and antibacterial activity of some new 2-(substituted phenyl sulfonamido)-6-substitutedbenzothiazoles. Indian J Heterocycl Chem. 2001;11:78-80.
39. Chandra Shekar B, Roy K, De AU. Synthesis of some new p-toluene sulfonamido glutaramides. Indian J Heterocycl Chem. 2001;10:237-8.
40. Ahmed B, Khan SA, Alam T. Synthesis and antihepatotoxic activity of some heterocyclic compounds containing the 1,4-dioxane ring system. Pharmazie. 2003;58(3):173-6. PMID 12685811.
41. Undheim K, Benneche T. In: Katritzky AR, Rees CW, Scriven EFV, McKillop A, editors. ComprehensiveHeterocyclicChemistryII. Vol. 6. Oxford: Pergamon Press; 1996. p. 93-231. doi: 10.1038/ja.2005.107, PMID 16506697.
42. Ramanatham VK, Gopal KR, Kotha VSR, Kumar Seshu. Facile synthesis and antimicrobial properties of 2-(substituted-benzylsulfanyl)-1h-benz-imidazoles. J Heterocycl Chem. 2009;42:1402-8.
43. Maeda H. SMANCS and polymer-conjugated macromolecular drugs: advantages in cancer chemotherapy. Adv Drug Deliv Rev. 1991;6(2):181-202. doi: 10.1016/0169-409X(91)90040-J.
44. Engler TA, Lynch KO, Chai W, Meduna SP. Cycloaddition reactions of 1,4-benzoquinone mono- and bisimides with styrenyl systems: new syntheses of nitrogen substituted azapterocarpans, pterocarpans, 2-aryl-2,3-dihydroindoles and -dihydrobenzofurans. Tetrahedron Lett. 1995;36(16):2713-6. doi: 10.1016/0040-4039(95)00375-M.
45. Engler TA, LaTessa KO, Iyengar R, Chai WY, Agrios K. Stereoselective syntheses of substituted pterocarpans with anti-HIV activity, and 5-aza-/5-thia-pterocarpan and 2-aryl-2,3-dihydrobenzofuran analogues. Bioorg Med Chem. 1996;4(10):1755-69. doi: 10.1016/0968-0896(96)00192-7, PMID 8931946.
46. Marmur J. A procedure for the isolation of deoxyribonucleic acid from microorganisms. Mol Biol. 1961;3:208-18.
47. Müller WEG, Rohde HJ, Steffen R, Maidhof A, Zahn RK. Potentiation of the effectiveness of bleomycin by A·T-specific DNA ligands *in vitro* as well as *in vivo*. Cancer Letters. 1975;1:127-32. doi: 10.1016/S0304-3835(75)95965-0.
48. Cohen G, Eisenberg H. Viscosity and sedimentation study of sonicated DNA-proflavine complexes. Biopolymers. 1969;8(1):45-55. doi: 10.1002/bip.1969.360080105.
49. Satyanarayana S, Dabrowiak JC, Chaires JB. Neither delta- nor lambda-tris(phenanthroline)ruthenium(II) binds to DNA by classical intercalation. Biochemistry. 1992;31(39):9319-24. doi: 10.1021/bi00154a001, PMID 1390718.
50. Kratz F, Nuber B, Weiß J, Keppler BK. Synthesis and characterization of potential antitumor and antiviral gallium(III) complexes of α-(N)-heterocyclic thiosemicarbazones. Synthesis and Reactivity in Inorganic and Metal-Organic Chemistry. 1991;21(10):1601-15. doi: 10.1080/15533179108020631.
51. Biradar NS, Kulkarni VH. A spectroscopic study of tin(IV) complexes with multidentate schiff bases. Journal of Inorganic and Nuclear Chemistry. 1971;33(11):3781-6. doi: 10.1016/0022-1902(71)80285-3.
52. Barry AL, Hoeprich PD, Saubolle MA. The antimicrobic susceptibility test: principles and practices. 4th ed. LBS, Lea and Febiger. Philadelphia; 1976. p. 180-93.
53. Thorn GW, Adams RD, Braunwald E, Isselbacher KJ, Petersdorf RG. Harrison's Principles of Internal Medicine. New York: McGraw-Hill Co; 1977.
54. Satyanarayana S, Dabrowiak JC, Chaires JB. Tris(phenanthroline)ruthenium(II) enantiomer interactions with DNA: mode and specificity of binding. Biochemistry. 1993;32(10):2573-84. doi: 10.1021/bi00061a015, PMID 8448115.
55. Moreno RG, Alipázaga MV, Gomes OF, Linares E, Medeiros MHG, Coichev N. DNA damage and 2′-deoxyguanosine oxidation induced by S(IV) autoxidation catalyzed by copper(II) tetraglycine complexes: synergistic effect of a second metal ion. J Inorg Biochem. 2007;101(5):866-75. doi: 10.1016/j.jinorgbio.2007.02.003, PMID 17383005.
56. Ghosh S, Barve AC, Kumbhar AA, Kumbhar AS, Puranik VG, Datar PA, Sonawane UB, Joshi RR. Synthesis, characterization, X-ray structure and DNA photocleavage by cis-dichloro bis(diimine) Co(III) complexes. J Inorg Biochem. 2006;100(3):331-43. doi: 10.1016/j.jinorgbio.2005.11.022, PMID 16412513.